Experimental study for the geogrid-reinforced embankment with clay cover under static and cyclic loading

Mengxi Zhang[1*], Hao Zhu[2], Longqing Chen[3], Akbar A Javadi[4]

[1]Professor, Department of Civil Engineering, Shanghai University, Shanghai, 200072, China. Email: mxzhang@i.shu.edu.cn.

[2]PhD, Department of Civil Engineering, Shanghai University, Shanghai, 200072, China. Email: zhuhao2747@shu.edu.cn.

[3]MSc, Department of Civil Engineering, Shanghai University, Shanghai, 200072, China. Email: lqchen1993@163.com.

[4]Professor, Department of Engineering, College of Engineering Mathematics and Physical Sciences, University of Exeter, Exeter, Devon EX4 4QF, UK. E-mail: A.A.Javadi@exeter.ac.uk.

Number of words:5238 (except Acknowledgement, References, Figures and Tables)

Number of tables: 6

Number of figures: 15

Experimental study for the geogrid-reinforced embankment with clay cover under static and cyclic loading

Abstract: This paper presents an analysis on a geogrid-reinforced embankment with clay-cover by model tests under static and cyclic loading. The deformation and failure surface inside the embankment were obtained by Particle Image Velocimetry (PIV). The test results showed that geogrids effectively improved the ultimate bearing capacity and reduced the vertical settlement and lateral displacement of reinforced embankment. The reinforcement effect increased with the increase of geogrid length, and the ultimate bearing capacity of the embankment reinforced with the longest geogrid was 51.9 kPa, which was 79% higher than that of unreinforced embankment. The wrapped clay formed an effective lateral constraint on the outward movement of the slope soil under pressure. When the reinforced embankment was damaged, the internal displacement significantly reduced, and the sliding surface in the middle of the embankment pointing to the foot of slope began to move into the embankment in an arc shape. In the cyclic loading test, the stress concentration effect inside embankment reduced by geogrid reinforcement. During each cycle, the earth pressure varied with a stable half-sine wave. The conclusions drawn from this study can provide an important fundamental data for the construction in geotechnical and road engineering.

Keywords: Geosynthetics; Model test; Cyclic loading; Deformation characteristics; Earth pressure

1. Introduction

With the continuous development of the traffic network, more and more roads are built in remote areas for further strengthen the connection between cities and villages. Different from high-speed railways, these roads need to be maintained at a lower cost. Although unpaved roads made of soil or gravel account for 80% of the global road network and play an important role in community road traffic, little related research focus on them [1]. In fact, traffic conditions have high requirements for road construction, so it is necessary to take reinforcement measures to improve the stability [2].

Considering the regional restriction and limited traffic conditions, geosynthetics reinforcement technology is widely used in road construction with low cost and high construction efficiency [3,4]. Many scholars conducted a large number of studies on the characteristics of reinforced soils through field tests, limit equilibrium analysis, or finite element numerical simulation and found that geosynthetics reinforcement significantly improved the structural stability and reduced the deformation of soil [5,6,7,8,9,10,11].

Specifically, geosynthetics such as geogrids play an important role in improving the properties of embankments due to good tensile properties. Its excellent applicability in reinforcement is mainly reflected in two aspects: (1) Provide passive resistance and increase binding force on the soil [12]. For embankment, the axial horizontal thrust generated by the filler from the centre to both sides reduces the bearing capacity of the vertical load, and then causes the lateral displacement of the filler. But the placement of geogrid can provide passive resistance, effectively improve the roughness of the interface and increase the binding force on the soil. (2) Suppress the arching of the soil and reduce the settlement of the pavement [13]. The coarse-grained filler in the transition section of the embankment will physically change its volume under the action of load and porosity. During this process, the slip and rolling of soil particles are closely related to the friction between particles. The geogrid can interlock with the soil particles to produce a more stable soil structure and occlude the soil particles with each other to control the soil, thus improving the settlement of embankment.

On the other hand, compacted soil is commonly used in transportation infrastructure. Experts have discussed the application of modified clay as highway construction materials [14,15]. Anaokar et al. [16] used lime-stabilized soil as capping material to control the expansion displacement of flexible pavement and effectively reduce the uneven deformation, and found that the permeability of clay decreased by more than 80%. Maigre et al. [17] conducted a field experiment on the road constructed by clay stabilized by 2% lime, and proved that lime treatment can improve the bearing capacity of the road and significantly reduce the settlement. In the actual engineering case, An [18] presented a case of full-scale study to evaluate the embankment with lime-treated clay as capping material and showed a good field performance during the operation of the embankment. Bicalho et al. [19] introduced the field monitoring of embankment constructed with lime-treated silty clay during four-years in the northeast of France. They focused on analysing the volumetric water content of each position of the embankment under natural climatic conditions and obtained in-situ soil water retention data, the results showed that a clay treated with 2% lime has a good field performance. However, the above research mainly focuses on the analysis of soil properties, rather than the stability of the whole embankment structure. In fact, the latter can provide a better basis for engineering practice.

Considering that in practical engineering, the embankment is mainly affected by traffic load, which is usually instantaneous and multifrequency [20]. Therefore, reasonable evaluation of slope deformation under cyclic loading is of great significance to ensure slope safety. Enomotoa and Sasaki [21] conducted a series of dynamic centrifugal model tests to evaluate the factors affecting the seismic performance of hillside embankment composed of sand or silt on the slope. It was found that the downslope driving force was increased due to the weight of embankment, and the larger base slope produced greater embankment deformation under cyclic loading. Zhang et al. [22] analysed the slope deformation under cyclic loading through model tests with different amplitudes and average pressures, and revealed that the potential slip surface was the key to slope failure.

Therefore, model tests are carefully carried out under laboratory conditions under cyclic loading. With regard to the studies already conducted, the number of reinforcement layers, length, and spacing between the reinforcements have a certain impact on the results [23]. For example, Choudhary et al. [24] evaluated the mechanical properties of strip foundation reinforced with geogrid, which was tested by changing the number of geogrid layers and layout depth. On this basis, modified clay with different thickness is used as test condition to cover the embankment. The modified clay on both sides of the slope limits the large lateral displacement of soil with weak cohesive force and strong fluidity, and improves the stability of the slope. The modified clay covered on the upper part of the embankment is used as an improvement layer to reduce the uneven settlement of the pavement. On the other hand, it is generally difficult to directly evaluate the deformation inside the embankment. Particle Image Velocimetry (PIV) technology can analyse the displacement of the same pixel between two images [25]. The application in this study can be used to reflect the tiny deformation between soils and form images to reveal the potential failure surface [26].

In summary, it is an innovative way to study a new embankment structure using geogrid reinforcement and clay cover. A series of model tests are carried out to study stability and deformation characteristics of geogrid-reinforced embankment covered with clay under static and cyclic loading. The conclusions drawn from the study possess important meanings for enriching the fundamental data in highway engineering.

2. Model tests

The research object of this study is the sand-filled embankment covered with clay. Figure 1 (a) shows that the traditional sand-filled embankment is only covered with geotextiles for isolation layer. However, geogrids are used in this study to reinforce the sand-filled embankment to improve bearing capacity and reduce settlement, as shown in Figure 1 (b). The relevant test system is shown in Figure 2. The strain-controlled dynamic and static loading apparatus (US GCTS's USTX-2000) was used for loading and measurement. The data acquisition system consisted of image data acquisition (PIV), soil pressure sensors and displacement data acquisition. The whole system had a maximum axial force of 10 kN, maximum displacement of 50 mm, and maximum frequency of 5 Hz under cyclic loading, with advantages of high precision, sensitive control etc.

2.1. Model test box

Considering the combination with the loading device and its stability during vibration caused by cyclic loading, the model box was selected as the container for embankment construction. The laboratory model box was cuboid, and the internal dimension was 600mm × 290mm × 400mm (length × width × height). In order to monitor and record the change process within the box during the test, the model box was embedded into a high-strength toughened glass of 25mm thick. The modified bottom plate of loading apparatus and model box were fixed as a whole by two metal columns. During the test, the DH5921 strain measurement system was used to collect the displacement data.

2.2. Test materials

2.2.1 Soil

The clayey soil used in this study was collected from a site along a national highway. Then the gathered clayey soil was dried in the oven at a temperature of 105 ℃ for 12 hours before being pulverized. The particle size distribution curve of the soil was tested by the commercial laser diffraction particle size analyser, as shown in Figure 3. Through undrained triaxial test under different confining pressures, it was determined that the internal friction angle and cohesion of clay were 22.3° and 19.8 kPa, respectively. A falling head permeability test was performed for clay as per ASTM D5084 [27], and the permeability of clay was 5.19×10^{-6} cm/s. Table 1 shows the physical and mechanical properties of the clayey soil used in this study, which is classified as clay of low plasticity (CL) according to ASTM D2487 [28].

The sand used in this study was locally available river sand, Shanghai China. Then the gathered sand was dried in the oven at a temperature of 105 ℃. The angle of internal friction of the sand tested was determined by undrained triaxial tests under different confining pressures, which was 35.7° at a relative density of 70%. The sand tested was classified as poorly graded sand (SP) in accordance with ASTM D2487 [28] and its physical properties was shown in Table 2. Figure 3 shows the particle size distribution curve of the sand tested by the commercial laser diffraction particle size analyser.

Appropriate ASTM standards were followed to determine the index properties of clay and sand such as specific gravity (ASTM D854) [29], liquid and plastic limit (ASTM D4318) [30], maximum dry density (ASTM D698) [31], etc.

2.2.2 Geogrid and Geotextile

A new type of fiberglass geogrid was used to reinforce the embankment throughout the test, which was made of glass fiber by weaving and coating, as shown in Figure 4. The length of each geogrid, both in the transverse and longitudinal directions was equal to 12 mm measured from the center-line of fiberglass strip. The widths of the vertical and horizontal strips were 4.5 mm and 2.25 mm, respectively. The properties of the fiberglass geogrid are shown in Table 3. According to ASTM D6637 [32] standard test method for tensile properties of geogrids, the transverse and longitudinal breaking strengths exceeded 7 kN/m at 5% strain. In addition, a woven geotextile was placed between sand and clay and used as isolation material in this study. The results of the tests of the geotextile according to ASTM D4595 [33] and other physical properties are illustrated in Table 4.

2.3. Cyclic loading

At present, most of the studies on applying traffic load in laboratory test are regular waveform vibration, among which half-sine wave and triangular wave are generally considered [34]. In this test, a half-sine wave cyclic loading was used to simulate traffic loading, as shown in Figure 5. Liu et al. [35] demonstrated that the influence of traffic load on subgrade can be accurately simulated when the frequency of cyclic load is 1 Hz, and the test results showed that the footing settlement remains stable after 20,000 cycles. After multiple parallel tests, 90% of the ultimate bearing capacity of unreinforced subgrade with underlying cave under static loading, i.e. 26.1 kPa, was taken as the loading amplitude of cyclic loading and the test frequency was 1 Hz. The cyclic load amplitude near the ultimate bearing capacity was helpful to analyze the reinforcement effect of geogrid in the ultimate state.

2.4. Principles of similitude

The similarity ratio is related to the engineering prototype and test model [36]. The test assumes that a highway with a width of 8.8 m, a height of 4 m, and slope ratio of 1:1.5. According to the similitude theory, the similitude coefficients, C_i, defined as the ratios of the prototype parameters i_p to the model parameters i_m [37], i.e.,

$$C_i = \frac{i_p}{i_m} \tag{1}$$

Considering the dimensions of the model test, the geometric similarity scale is determined to be C_L=20. The similarity ratio of bulk-density is C_γ=1, and the similarity parameters are shown in Table 5.

In the plate load test, the boundary effect was closely related to the size of the loading plate and model [38]. Michalowski and Shi [39] conducted a plate loading test and found that the boundary effect was insignificant when the width and height of the model were close to 10 and 6 times the width of the loading plate. Similarly, Chen et al. [40] performed plate load tests on transparent soil models with width and height of 10 and 6 times the plate width, and the results were consistent with the numerical simulation analysis. In this study, the dimensions of the model were 600 mm × 290 mm × 333/343 mm (length × width × height) and the dimensions of the loading plate were 280 mm × 60 mm (length × width). The dimensions are close to the appropriate range with references from the literature. So the influence of boundary effect can be considered insignificant in this experiment.

2.3. Test Program

The instruments and model box used in the test were placed in the mechanical laboratory. Before sample preparation, Low friction silicone grease was used to minimize possible friction between the walls of the test box and the assembled soils. Zhang et al. [41] compacted sand to construct the foundation of embankment model with a relative density of 0.7 and obtained reliable test data. In this test, 100 mm thick fill was laid at the bottom of the model box as embankment foundation. The model was established by static compaction of sand layer by layer. In this process, each layer was compacted to a relative density of 0.8 and a depth of 40 mm, totaling 5 layers. Once the soil reached the height of a reinforcement layer, the soil surface was leveled to lay a layer of geogrid. The process was repeated until the total thickness of the soil reached the design height, and the test scheme is shown in Figure 6. When the sand filling completed, the surface was covered with geotextile then wrapped with a certain thickness of clay. According to previous research, 2% lime mixed clay was used in embankment construction and showed good performance [19]. Through repeated tests, this study adopted clay with water content of 18.6% mixed with 2% lime as embankment cover layer, which has a better compaction effect. Table 6 shows the corresponding test conditions, including five groups of tests, which were carried out independently, with a non-reinforced condition being set as a control sample.

Furthermore, the embankment reinforced with two layers of 200 mm geogrids and covered with 33 mm thick clay was taken as test condition 2, and test conditions 3, 4 and 5 increased the layers, length and thickness of the geogrids based on test condition 2, respectively. During the experiment, the displacement meters were placed on the slope of the embankment at intervals of 100mm and on the top of the embankment at intervals of 40mm to measure the displacement characteristics, with a total of 6 counts.

In the static loading test, a load was applied on the middle of the road surface. During the loading process, the test was stopped when the displacement suddenly changed and the embankment suffered overall shear failure. The displacement monitoring test of Particle Image Velocimetry (PIV) was conducted, which was to further reveal the deformation and displacement of sand inside the embankment.

3. Results and Discussion

3.1. Static loading tests of embankment

3.1.1 Ultimate bearing capacity

Figure 7 shows the bearing pressure and displacement curve of the embankment under static loading. On the whole, with the increase of vertical load, the linear relationship between embankment bearing pressure and displacement firstly increases with a certain slope. During this process, the sand is gradually compacted, resulting in a larger contact interface with the reinforcement, thus increasing the interfacial friction and forming a larger shear strength. When the loading reaches some points, generating larger plastic strains, and the shear failure appears in the embankment. The compression curve starts to turn down sharply, marking the complete loss of strength in the embankment. In this situation, the points corresponding to the swift change of slope are called the ultimate bearing capacity. For the case of the unreinforced embankment, the ultimate bearing capacity is only 29 kPa. However, with the reinforcement of geogrid, the embankment has a better performance and the bearing capacity is significantly improved. The maximum bearing capacity of the embankment reinforced with the longest geogrid is 51.9 kPa, which is 79% higher than that of the unreinforced embankment. This is because the friction and locking force between geogrids and sand reduces the stress concentration effect of the embankment, and the coupling effect between geogrids is further improved with the increase of reinforcement layers and length, thereby improving the ultimate bearing capacity of the embankment. On the other hand, the clay cover strengthens the performance of pavement and reduces the footing settlement by 20%, which is significant to improve the deformation characteristics of sand-filled embankment, as shown in Figure 8. Furthermore, increasing the thickness of clay cover can provide lateral restraint of sand core and improve the ultimate bearing capacity of the embankment to a certain extent, which is 54% higher than that of the unreinforced embankment (test condition 5).

3.1.2 Deformation

In order to analyse the deformation of the reinforced embankment under different test conditions, displacement sensors are installed on the surface of the embankment slope and pavement, and the specific location distribution is shown in the Figure 6. Figure 9 (a) shows the significant lateral deformation of the slope. Due to the interaction between the sand and the geogrid, the lateral displacements at different positions on the slope are quite different. For the unreinforced sand embankment, the deformation is mainly reflected in the middle part, reaching 24.6 mm. With geogrid reinforcement, the deformation decreases significantly in the upper part of embankment, but it increases gradually along the slope. At the same measuring point (No. $1^{\#}$), the deformation of the unreinforced embankment is 14.3 mm, while that of the embankment reinforced with four layers of geogrid is 4.5 mm, which is reduced by 68%. The best deformation control of measuring point No. $2^{\#}$ is the embankment reinforced by geogrid with a length of 280 mm, which is 42% less than that of unreinforced embankment, showing a good ability to restrain soil deformation. It is also noted that the deformation of the pavement is the largest in the No.$5^{\#}$ area, followed by the place near the slope. As shown in Figure 9 (b), the pavement deformation of the embankment after reinforcement has been reduced, and the embankment reinforced with the longest geogrid has the best effect compared to other test conditions. This is because in the reinforced embankment system, the interfacial friction effect between the soil and the reinforcement can effectively restrain the lateral deformation of the soil, which makes it difficult for the soil on both sides of the upper part to produce large displacement. In the unreinforced embankment system, the force inside the embankment transmits vertically, which leads to the increase of displacement in middle part. When the shear stress in the embankment approaches the shear strength value, the shear failure zone appears in the embankment and further develops into the foot of the slope, resulting in a large displacement at the bottom, and the failure sliding surface of circular arc is formed inside the embankment. For the settlement of the pavement, the geogrid and sand located closest to the top of embankment are compacted by load, and then further develop into lateral pressure on the transverse ribs of the geogrid, resulting in stress concentration in the reinforcement arrangement layer. Therefore, the No.$5^{\#}$ area closest to the loading position has the largest settlement, and the No.$6^{\#}$ area also has a large settlement due to stress concentration.

3.1.3 Failure form

In order to clearly obtain the failure morphology of the geogrid-reinforced embankment under static loading, two-dimensional Particle Image Velocimetry (PIV) testing technology was used to track and photograph the movement of sand particles inside the embankment. Furthermore, the displacement changes and failure modes in the cross-section of the model box were recorded through the pin fixed-point monitoring test. Due to the clay part with smaller particles was difficult to identify, a part of the sand core was treated, and the related displacement scalar change of the reinforced embankment was shown in Figure 10 (a). It can be seen that when the embankment is damaged, the sliding surface at the sand core is a broken line composed of a vertical straight line passing through the midpoint of the road surface and a diagonal line pointing to the foot of the slope inside the embankment. The soil is extruded outward along the outer layer of the upper part of the embankment. In addition, the maximum displacement at the junction of the clay and sand core on the top of the slope is 8.05 mm and decreases gradually towards the inside of the embankment. Figure 10 (b) shows the displacement scalar diagram of the embankment with maximum ultimate bearing capacity (test condition 4). The maximum displacement is 6.54 mm in the middle of embankment, which is 18.7% lower than that of the unreinforced embankment, and the displacement decreases gradually towards the outside of embankment. The sliding surface in the middle of the embankment which points to the foot of slope began to become arc-shaped and moves to the inside of embankment, and the wrapped clay forms an effective lateral restriction on the soil moving outward under pressure. This means that the overall strength of the reinforced embankment has been effectively improved, and the soil has obvious confining effect after being squeezed, which greatly reduces the displacement and deformation of the embankment. Both the number of layers of geogrid and the length of geogrid affect the sliding surface and developing displacement area of the embankment. With the increase of reinforcement layers, the interlocking effect of the geogrid on the soil and the stress deformation of the geogrid greatly increase the shear strength of soil and limit the deformation of soil. While the length of geogrid increases, the sliding surface is obviously affected, and the diffusion in the developing displacement area is obviously restrained, so that the reinforcement can be brought into full play.

Figure 11 (a) shows the displacement vector during failure according to the marked points of the unreinforced embankment before and after loading. It shows that when the embankment is damaged, the sand core and the bound soil move along the slope from inside to outside, and there is obvious displacement in the middle and top of the slope. The ultimate bearing capacity of the unreinforced embankment is small, so the displacement in the embankment is quickly transmitted to the top and middle of the slope, and the marking points in the embankment produce different displacements along the direction to the outside of the embankment. According to the test results in Figure 11 (b), it can be clearly seen that the marking points of each layer in the embankment after being reinforced by geogrid move obviously from inside to outside, and the amplitude is larger than that of the unreinforced embankment. Besides, the direction gradually changes from the lower right to the horizontal right. This shows that the interlocking effect between soil and geogrid and the tensile capacity from geogrid itself greatly increase the shear strength of the embankment and limit its deformation.

3.2. Cyclic loading tests of embankment

3.2.1 Ultimate bearing capacity

In order to analyse the influence of cyclic load on the bearing capacity of the embankment, the embankment was first subjected to cyclic loading for 20000 cycles under different amplitudes and then monotonic load was applied until the whole embankment failure. All tests were conducted independently, totaling 25 times. It can be seen from Figure 12 that the ultimate bearing capacity of the unreinforced embankment decreases with the increase of cyclic load amplitude and is lower than its value under static loading. However, the ultimate bearing capacity of the embankment strengthened by geogrid has improved significantly and continues to increase with the increase of cyclic loading amplitude, exceeding the ultimate bearing capacity under static loading. A comprehensive evaluation of all test conditions shows that the best reinforcement effect is achieved under test condition 4, which is also consistent with the static loading test. The results show that the possibility of sand shear failure increases when cyclic loading is applied to unreinforced embankment. Due to the test sand is classified as poorly graded sand, after the geogrid reinforced sand embankment is subjected to cyclic load, the sand recombines and increases the contact area and friction force with geogrid. Therefore, the locking effect of the soil makes the geogrid have an initial stretching effect, which further exerts its binding force on sand and enhances the reinforcement effect. In this way, the stress concentration effect of sand is reduced and ultimate bearing capacity of embankment is greatly improved. With the increase of geogrid length and number of layers, this effect becomes more significant.

It is worth noting that the ultimate bearing capacity of the unreinforced embankment is stable around 25 kPa under different cyclic load amplitudes, which is related to the selection of conventional cyclic load amplitude (26.1 kPa) in Chapter 2.3. Therefore, part of the results can also be regarded as the pre-experiment of the experimental scheme design.

3.2.2 Deformation

In order to study the deformation characteristics of the embankment under cyclic loading, 90% of the ultimate bearing capacity of the unreinforced embankment under static loading, i.e. 26.1 kPa, is taken as the appropriate load amplitude. At the same time, the loading frequency is 1 Hz, and the number of cycles is 20,000. The related test results are shown in Figure 13. It shows that the vertical cumulative settlements under cyclic loading are vary with the number of cycles. Under different test conditions, the cumulative vertical settlement of the embankment fast increases firstly, and then tends to slowly rise with the increase of cycle. The demarcation points of cycle from fast to slow are approximately 5000 times. In addition, it can be seen that the cumulative vertical settlement of the unreinforced embankment is significantly higher than that of the reinforced embankment under cyclic loading. In the first 5,000 cycles, the increase rate of the vertical cumulative settlement of the unreinforced embankment is significantly higher than that in the reinforced embankment. After 5,000 cycles, the cumulative vertical settlement in test condition 1 is 1.4 times bigger than that in working condition 2, and is 1.1 times bigger than that in test condition 3. It illustrates that under cyclic loading, increasing the number of reinforced layers has a great influence on the cumulative vertical settlement of the embankment. Furthermore, the increase of clay-cover thickness has effect on the embankment settlement but less than the effect caused by the number and length of geogrid layers. The results show that increasing the length and number of geogrids can provide greater tensile stress to soil, which is more conducive to the stability of embankment under cyclic loading. At the same time, the increase of the thickness of clay cover will improve the lateral restraint of embankment and control the deformation of the embankment, but the effect is not as good as that for increasing the length of geogrid.

Based on the above test results of pavement settlement under cyclic loading, the representative test cases 2, 4 and 5 are selected for comparison, and the cumulative displacement of the slope under different geogrid reinforcement lengths and thickness of clay cover is shown in Figure 14. It shows that the lateral cumulative displacement at the top of the slope increases with increasing the length of geogrid, while the lateral displacement at the middle and bottom of the slope decreases. This is because increasing geogrid length will increase the anchorage length of geogrid in sand, and the sand and geogrid are further compressed under cyclic loading. Therefore, the stress is mainly concentrated on the top reinforced geogrid near the loading point, and the deformation mainly occurs at the top of the slope, while the cumulative deformation transmitted to the foot from the top of the slope is relatively small. At the same time, with the increase of the thickness of clay cover, the lateral cumulative deformation of the top of the slope decreases, while it keeps the same at the middle and bottom of the slope.

3.2.3 Earth Pressure

According to the test program in Section 2.3, five earth pressure sensors are placed in the upper part of the embankment to measure the earth pressure distribution inside the embankment under cyclic loading. Figure 15 shows the earth pressure variation of the embankment within 90 to 100 cycles during the loading process. In each cycle, the earth pressure inside the embankment presents a half-sine waveform. For the unreinforced embankment, the earth pressure decreases with the increase of vertical depth, as shown in Figure 15(a). In the horizontal direction, it is the largest at No.3$^{\#}$, which is closest to the loading position and decreases to both sides. However, after geogrid reinforcement, the earth pressure measured in the embankment increases significantly, especially at the deepest measuring point called No.5$^{\#}$, which proves that the reinforced embankment has higher strength. This is because the unreinforced embankment is mainly deformed at the top and middle of the slope, and the stress is also concentrated in these places. The geogrid reinforced embankment can improve the overall shear strength, and reduce the stress concentration effect in the embankment. While the measurement point No.4$^{\#}$ is closer to the side slope, and most of the stress is released due to soil deformation.

4. Conclusions

In this paper, a clay-covered embankment reinforced by geogrid is proposed. By controlling the number of geogrid layers, the length of geogrids and the thickness of clay, the mechanical and deformation characteristics of the embankment are analysed. The following conclusions can be drawn from the results:

(1) In the static loading experiment, the bearing capacity of the embankment is significantly improved by geogrid, and the reinforcement effect increases with the increase of geogrid layers. The maximum ultimate bearing capacity of the

embankment strengthened with two layers of geogrids with a length of 280 mm is 51.9 kPa, which is 79% higher than that of the unreinforced embankment. When the embankment is damaged, the sliding surface starts to be curved and moves to the inside of the embankment.

(2) The settlement of embankment under static loading is mainly reflected in the middle of the pavement and the geogrid reinforcement can effectively improve the deformation. For the slope of unreinforced embankment, the maximum displacement is 14.3 mm at No.1 measuring point, and it decreases by 68% after four-layer geogrid reinforcement. On the whole, the length of geogrid has the greatest influence on the reinforcement effect. PIV accurately reflects the deformation law of soil inside the embankment. Under the reinforcement of double-layer geogrids with a length of 280 mm, the maximum displacement inside the embankment is 6.54 mm, which is 18.7% lower than that of the unreinforced embankment.

(3) In the cyclic loading test of embankment, the ultimate bearing capacity of unreinforced embankment decreases with the increase of cyclic load amplitude. For the geogrid-reinforced embankment, the larger cyclic load amplitude leads to the closer combination of soil and geogrid, which improves the bearing capacity of the embankment. The vertical settlement of the embankment increases with the increase of cycle and tends to be stable after 5000 numbers of cycle. The clay cover effectively limits the large deformation of soil and reduces the settlement of the pavement.

(4) For the unreinforced embankment, the earth pressure is mainly concentrated in the upper part. Geogrid reinforcement effectively reduces stress concentration, and the earth pressure increases in the lower part of the embankment. In the horizontal direction, the earth pressure in the middle of the embankment is the largest and decreases to both sides. In each cycle, the earth pressure presents a half-sine wave, which is consistent with the cyclic load waveform.

Authorship contribution statement

All authors contributed in the conceptualization, methodology, manuscript writing and editing.

Acknowledgement

The authors thank the Funding received from the National Natural Science Foundation of China under grant No. 41372280.

Declarations

Conflict of interest. We would like to confirm that this work is original and has not been published elsewhere. All authors have read and approved the manuscript being submitted and agree to its submittal to this journal. We have no conflicts of interest to disclose.

References

1. Burrow, M.P.N., Evdorides, H., Ghataora, G.S., et al., 2016. The evidence for rural road technology in low-income countries. Transport 169, 366–377.
2. Hufenus, R., Rueegger, R., Banjac, R., et al., 2006. Full-scale filed tests on geosynthetic reinforced unpaved roads on soft subgrade. Geotextiles and Geomembranes 25, 21–37.
3. Jia, M.C., Zhu, W.K., Xu, C., 2021. Performance of a 33m high geogrid reinforced soil embankment without concrete panel. Geotextiles and Geomembranes 49, 122-129.
4. Singh, M., Trivedi, A., Shukla, S.K., 2022. Evaluation of geosynthetic reinforcement in unpaved road using moving wheel load test. Geotextiles and Geomembranes 50, 581-589.
5. Jewell, R.A., 1991. Application of revised design charts for steep reinforced slopes. Geotextiles and Geomembranes 10, 203-233.
6. Sharma, J.S., Bolton, M.D., 1996. Centrifuge modelling of an embankment on soft clay reinforced with a geogrid. Geotextiles and Geomembranes 14, 1-17.
7. Bathurst, R.J., Vlachopoulos, N., Walters, D.L., Burgess, P.G., Allen, T.M., 2006. The influence of facing stiffness on the performance of two geosynthetic reinforced soil retaining walls. Canadian Geotechnical Journal 43, 1225-1237.
8. Allen, T.M., Bathurst, R.J., Holtz, R.D., Walters, D., Lee, W.F., 2003. A new working stress method for prediction of reinforcement loadings in geosynthetic walls. Canadian Geotechnical Journal 40, p.976-994.
9. Klar, A., Sas, T., 2009. Rational approach for the analysis of segmental reinforced soil walls based on kinematic constraints. Geotextiles and Geomembranes 27, 332-340.
10. Wang, F., Miao, L., 2009. A proposed lightweight fill for embankments using cement-treated Yangzi River sand and expanded polystyrene (EPS) beads. Bulletin of Engineering Geology and the Environment 68, 517-524.
11. Xu, C., Liang, C., Shen, P., 2019. Experimental and theoretical studies on the ultimate bearing capacity of geogrid-reinforced sand. Geotextiles and Geomembranes 47 (3), 471- 428.
12. Esmaeili, M., Naderi, B., Neyestanaki, H.K., Khodaverdian, A., 2018. Investigating the effect of geogrid on stabilization of high railway embankments. Soils and Foundations 58, 319-332.
13. Saran, S., Kumar, S., Garg, K., 2008. Model tests on eccentrically and obliquely loaded footings resting on reinforced sand. International Journal of Geotechnical Engineering. 2, 179-197.
14. Kampala, A., Horpibulsuk, S., Chinkullijniwat, A., et al., 2013. Engineering properties of recycled Calcium Carbide Residue stabilized clay as fill and pavement materials. Construction and Building Materials 46, 203-210.
15. Gupta, D., Kumar, A., 2017. Performance evaluation of cement-stabilized pond ash-rice husk ash-clay mixture as a highway construction material. Journal of Rock Mechanics and Geotechnical Engineering 9, 159-169.
16. Anaokar, M., Mhaiskar, S., 2020. Experimental and numerical assessment of efficacy of lime stabilized capping material in controlling swelling displacements within flexible pavement embankments. Heliyon 6, e04961.
17. Maigre, I.D., Morsel, A., Briancon, L., et al., 2022. Uses of Usumacinta River sediments as a

sustainable resource for unpaved roads: An experimental study on a full-scale pilot unit. Transportation Engineering 9 100136.

18. An, N., 2017. Numerical investigation of soil-atmosphere interaction: application to embankments of treated soils Ph. D. Thesis Paris: Université Paris-Est.
19. Bicalho, K.V., Boussarfir, Y., Cui, Y.J., 2018. Performance of an instrumented embankment constructed with lime-treated silty clay during four-years in the Northeast of France. Transportation Geotechnics 17, 100-116.
20. Chai, J.C., Miura, N., 2002. Traffic-load-induced permanent deformation of road on soft subsoil. Journal of Geotechnical and Geoenvironmental Engineering 128 (11), 907-916.
21. Enomotoa, T., Sasaki, T., 2015. Several factors affecting seismic behaviour of embankments in dynamic centrifuge model tests. Soils and Foundations 55 (4), 813-828.
22. Zhang, G., Wang, T.L., Luo, F.Y., 2022. Simplified method for analyzing soil slope deformation under cyclic loading. Journal of Rock Mechanics and Geotechnical Engineering 14, 1967-1976.
23. Yoo, C., 2001. Laboratory investigation of bearing capacity behavior of strip footing on geogrid reinforced sand slope. Geotextiles and Geomembranes 19, 279–298.
24. Choudhary, A.K., Jha, J.N., Gill, K.S., 2010. Laboratory investigation of bearing capacity behavior of strip footing on reinforced fly ash slope. Geotextiles and Geomembranes 28, 393–402.
25. Guo, Y., Markine, V., Zhang, X., Qiang, W., Jing, G., 2019. Image analysis for morphology, rheology and degradation study of railway ballast: A review. Transportation Geotechnics 18, 173–211.
26. Burke, T.S.D.S., Elshafie, M.Z.E.B., 2021. Geosynthetic-reinforced soils above voids: Observation of soil and geosynthetic deformation mechanisms. Geotextiles and Geomembranes 49, 1-18.
27. ASTM, 2016. Standard test methods for measurement of hydraulic conductivity of saturated porous materials using a flexible wall permeameter. D5084. West Conshohocken, PA.
28. ASTM, 2011. Standard Practice for Classification of Soils for Engineering Purposes. D2487. West Conshohocken, PA.
29. ASTM, 2016. Standard Test Methods for Specific Gravity of Soil Solids by Water Pycnometer. D854. West Conshohocken, PA.
30. ASTM, 2010. Standard Test Methods for Liquid Limit, Plastic Limit, and Plasticity Index of Soils. D4318. West Conshohocken, PA.
31. ASTM, 2012. Standard Test Methods for Laboratory Compaction Characteristics of Soil Using Standard Effort. D698. West Conshohocken, PA.
32. ASTM, 2015. Standard Test Method for Determining Tensile Properties of Geogrids by the Single of Multi-Rib Tensile Method. D6637. West Conshohocken, PA.
33. ASTM, 2017. Standard Test Method for Tensile Properties of Geotextiles by the Wide-Width Strip Method. D4595. West Conshohocken, PA.
34. Razouki, S.S., Schanz, T., 2011. One-dimensional consolidation under haversine repeated loading with rest period. Acta Geotechnica 6, 13-20.
35. Liu, K.F., Feng, W.Q., Cai, Y.H., Xu, H., Wu, P.C., 2023. Physical model study of pile type effect on long-term settlement of geosynthetic-reinforced pile-supported embankment under traffic loading. Transportation Engineering 38, 100923.
36. Xu, S.S., Lei, H., Li, C., Liu, H.Q., Lai, J.X., Liu, T., 2021. Model test on mechanical

characteristics of shallow tunnel excavation failure in gully topography. Engineering Failure Analysis 119, 104978.

37. Huang, F., Zhu, H., Xu, Q., Cai, Y., Zhuang, X., 2013. The effect of weak interlayer on the failure pattern of rock mass around tunnel-Scaled model tests and numerical analysis. Tunnelling and Underground Space Technology 35, 207-218.
38. Kumar, A., Saran, S., 2003. Closely spaced footings on geogrid reinforced sand. Journal of Geotechnical and Geoenvironmental Engineering 129 (7), 660-664.
39. Moghaddas Tafreshi, S.N., Dawson, A.R., 2010. Comparison of bearing capacity of a strip footing on sand with geocell and with planar forms of geotextile reinforcement. Geotextiles and Geomembranes 28, 72-84.
40. Chen, J.F., Guo, X.P., Sun, R., Rajesh, S., Jiang, S., Xue, J.F., 2021. Physical and numerical modelling of strip footing on geogrid reinforced transparent sand. Geotextiles and Geomembranes 49, 399-412.
41. Zhang, M.X., Qiu, C.C., Javadi, A.A., Zhang, S.L., 2014. Model tests on reinforced sloped embankment with denti-strip inclusions under monotonic loading. KSCE Journal of Civil Engineering 18 (5), 1342-1350.

List of figures

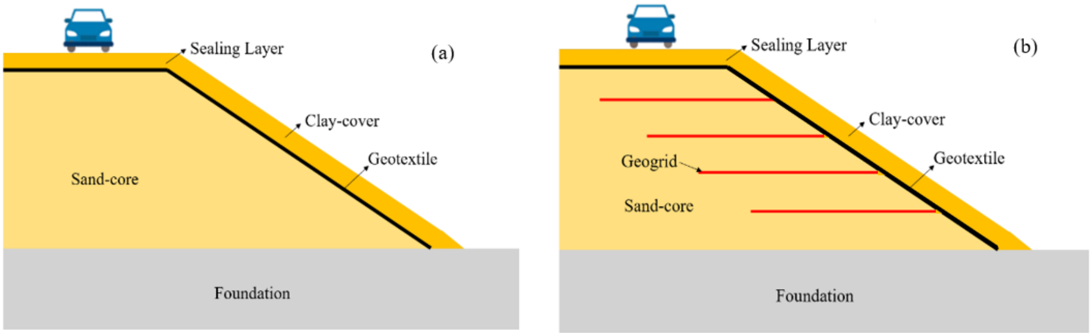

Figure 1. The structure of sand-filed embankment covered by clay (a) Geotextile is used as isolation layer (b) Reinforced with geogrid

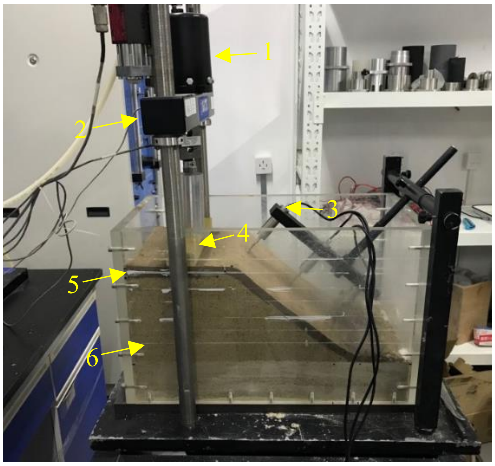

Figure 2. Model test system. 1. Load-cylinder; 2. Reaction frame; 3. Displacement meter; 4. Loading plate; 5. Clay cover; 6. Sand

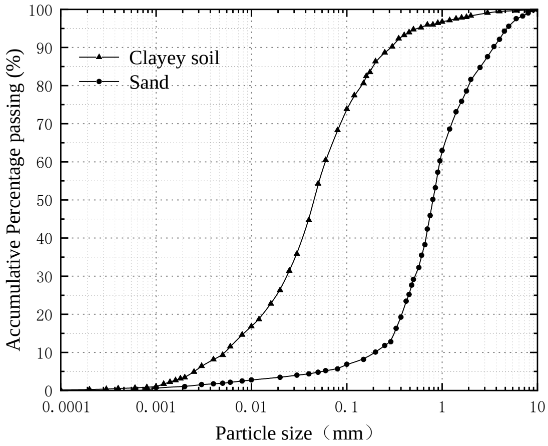

Figure 3. Particle size distribution of the clayey soil and sand

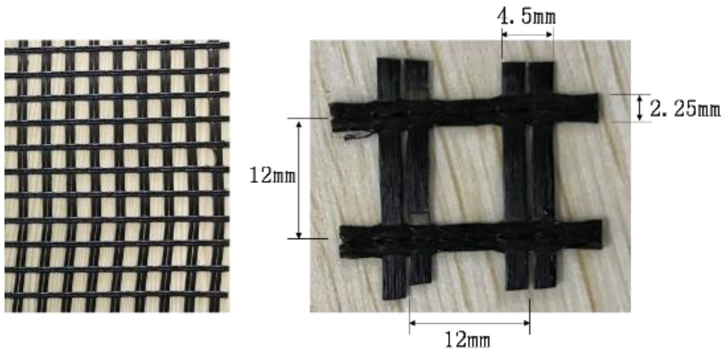

Figure 4. Fiberglass geogrid

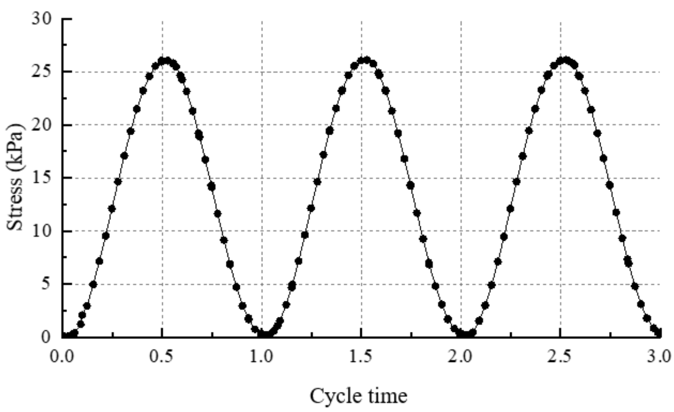

Figure 5. Waveform of cyclic load

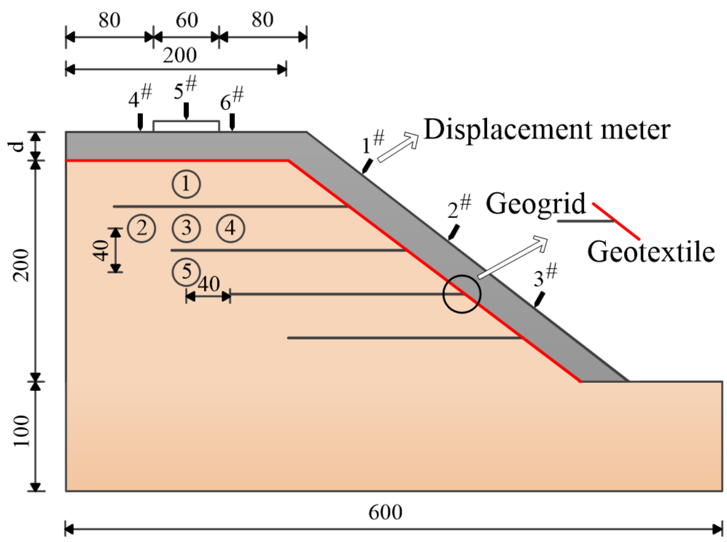

Figure 6. Model size of the embankment model (dimensions in mm)

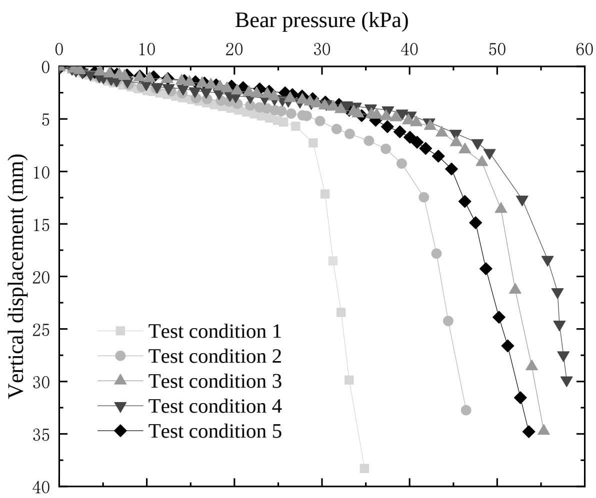

Figure 7. Bearing pressure and displacement curve of the embankment under different test conditions

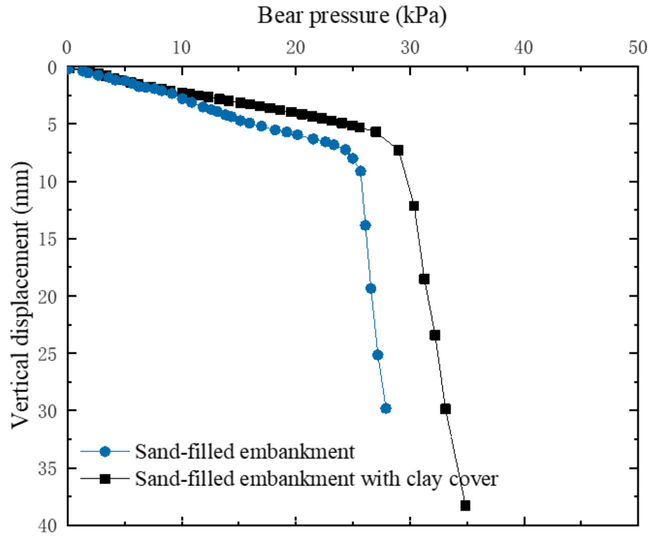

Figure 8. The bearing pressure-displacement relationship curve of embankment

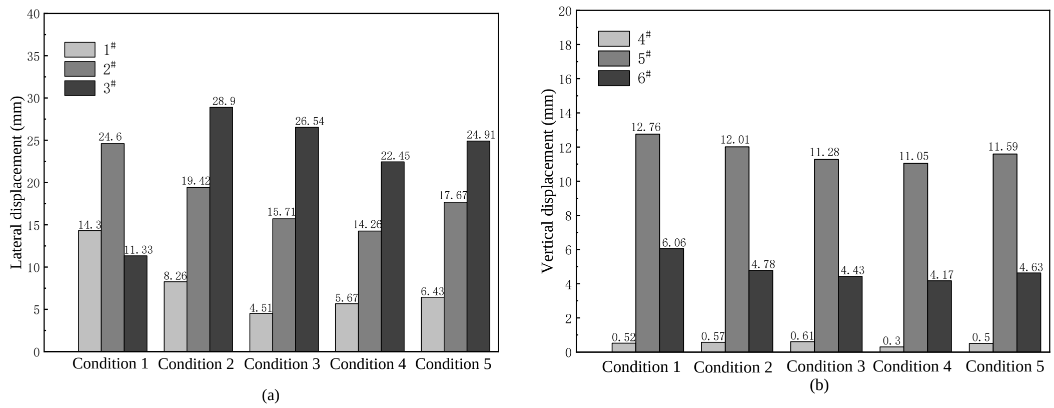

Figure 9. Displacement of reinforced embankment under different test conditions (a) Slope (b) Pavement

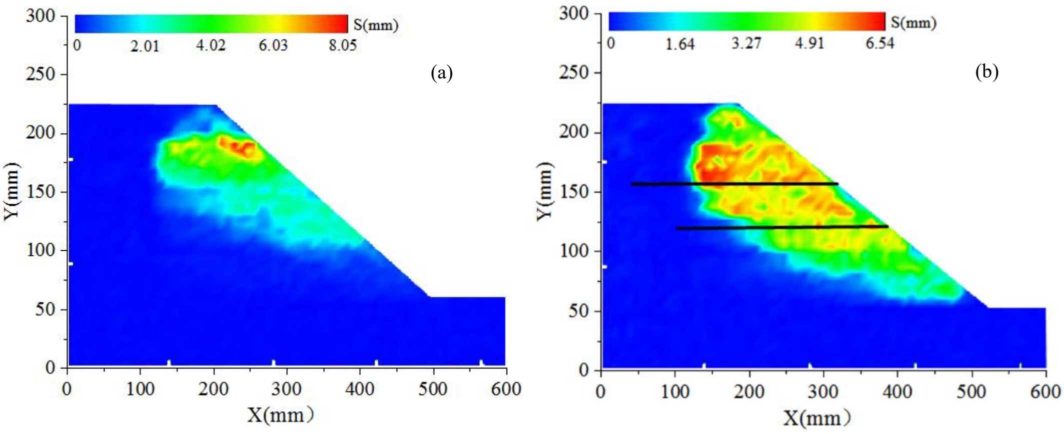

Figure 10. Displacement scalar diagram of sand core (a) Test condition 1 (b) Test condition 4

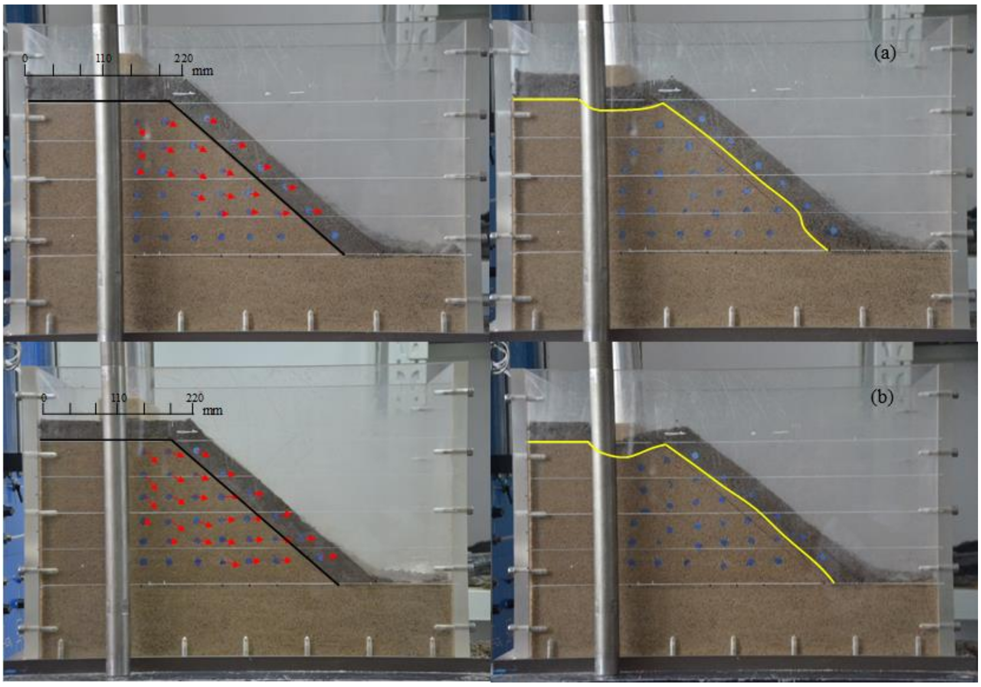

Figure 11. Photograph for footing displacement and vector change of embankment under different test conditions (a) Teat condition 1 (b) Test condition 4

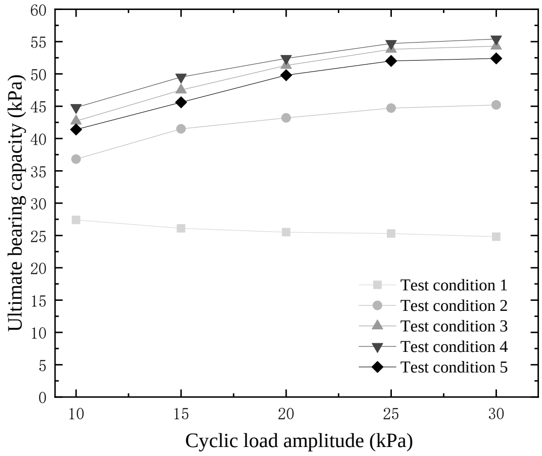

Figure 12. Curve of ultimate bearing capacity of embankment with cyclic load amplitude under different test conditions

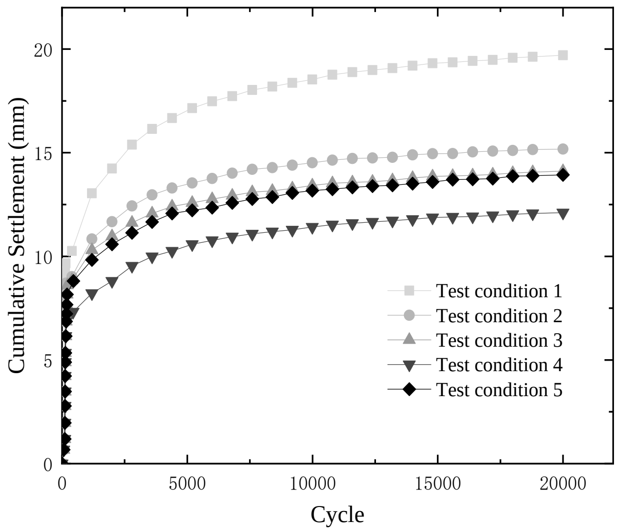

Figure 13. Curve of cumulative vertical displacement of pavement with cycle under different test conditions

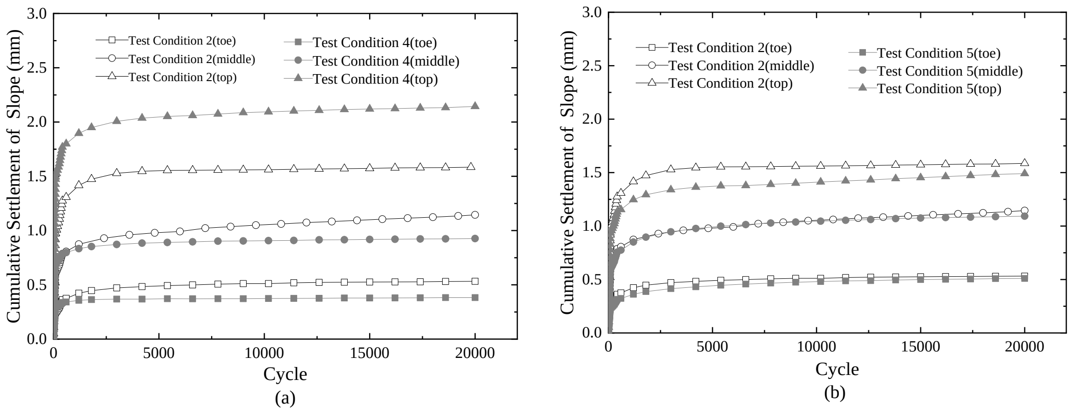

Figure 14. The cumulative deformation of slope in lateral direction under different test conditions varies with cycle time (a) Cumulative displacement of slope with different reinforcement lengths (b) Cumulative displacement of slope with different clay thickness

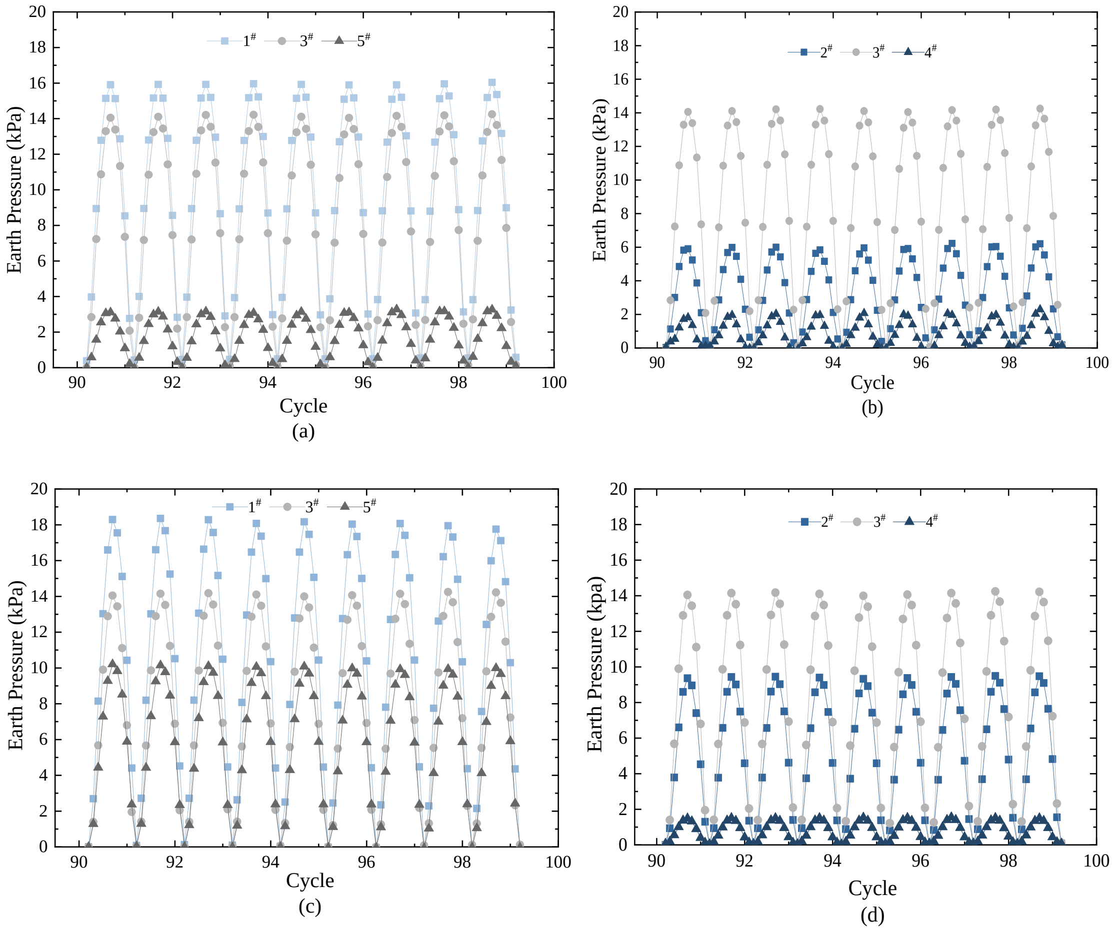

Figure 15. Curve of earth pressure with number of cycles under different test conditions (a) Longitudinal earth pressure distribution in test condition 1 (b) Transverse earth pressure distribution in test condition 1 (c) Longitudinal earth pressure distribution in test condition 4 (d) Transverse earth pressure distribution in test condition 4

List of tables

Table 1 Physical and mechanical properties of clayey soil

Properties	Value
Liquid limit (%)	35.06
Plastic limit (%)	23.35
Plastic index (%)	11.71
Unit density (kN/m^3)	16.8
Optimum water content (%)	20.68
Specific gravity (Gs)	2.62
Internal friction angle (°)	22.3
Cohesion (kPa)	19.8
Coefficient of uniformity (Cu)	10.71
Coefficient of curvature (Cc)	1.64

Table 2 Physical properties of test sand

Properties	Value
D_{10} (mm)	0.21
D_{30} (mm)	0.52
D_{60} (mm)	0.95
Coefficient of uniformity (Cu)	4.52
Coefficient of curvature (Cc)	0.20
Specific gravity (Gs)	2.74
Maximum dry density (g/cm^3)	1.92
Minimum dry density (g/cm^3)	1.58

Table 3 Physical properties of fiberglass geogrid

Properties	Unit	Value
Grid size	mm	12×12
Transverse tensile strength (2% strain)	kN/m	2.8
Longitudinal tensile strength (2% strain)	kN/m	4
Transverse tensile strength (5% strain)	kN/m	5.4
Longitudinal tensile strength (5% strain)	kN/m	7
Ultimate tensile strength (6% strain)	kN/m	11

Table 4 Physical properties of geotextile

Properties	Unit	Value
Axial load capacity	kN	5.5
Extension at failure	%	4.8
Thickness	mm	1.5
Longitudinal tensile strength (2% strain)	kN/m	13.6
Unit mass	kg/m^2	0.1

Table 5 Similarity parameter between the model and the original structure

Parameters	Definition	Relations	Similarity ratio
Stress	$C_\sigma = \sigma_p/\sigma_m$	$C_\sigma = C_\gamma C_L$	20
Strain	$C_\varepsilon = \varepsilon_p/\varepsilon_m$	$C_\varepsilon = C_\mu$	1
Cohesion	$C_c = C_p/C_m$	$C_c = C_\sigma$	20
Density	$C_\gamma = \gamma_p/\gamma_m$	$C_\gamma = C_\sigma/C_L$	1
Elasticity modulus	$C_E = E_p/E_m$	$C_E = C_\sigma/C_\varepsilon$	20
Poisson's ratio	$C_\mu = \mu_p/\mu_m$	$C_\mu = C_\varepsilon$	1
Friction coefficient	$C_\varphi = \varphi_p/\varphi_m$	$C_\varphi = C_\mu$	1

C represents the similarity scale. Subscript, p represents the prototype, m represents the prototype model, σ represents stress, ε represents strain, c represents cohesion, γ represents bulk density, E represents modulus of elasticity, μ represents Poisson's ratio, φ represents angle of internal friction.

Table 6 Different test conditions of the study

Test conditions	Reinforced layer N	Length of geogrid reinforcement (mm)	Thickness of clay-cover d (mm)	Depth of the first geogrid in sand (mm)	Spacing (mm)
1	0	0	33	0	0
2	2	200	33	70	40
3	4	200	33	40	40
4	2	280	33	70	40
5	2	200	43	70	40